Article

Unsteady Magnetohydrodynamics (MHD) Flow of Hybrid Ferrofluid Due to a Rotating Disk

Iskandar Waini [1], Najiyah Safwa Khashi'ie [1],*, Abdul Rahman Mohd Kasim [2], Nurul Amira Zainal [1], Khairum Bin Hamzah [1], Norihan Md Arifin [3,4] and Ioan Pop [5]

[1] Fakulti Teknologi Kejuruteraan Mekanikal dan Pembuatan, Universiti Teknikal Malaysia Melaka, Hang Tuah Jaya, Durian Tunggal 76100, Melaka, Malaysia; iskandarwaini@utem.edu.my (I.W.); nurulamira@utem.edu.my (N.A.Z.); khairum@utem.edu.my (K.B.H.)
[2] Centre for Mathematical Sciences, College of Computing and Applied Sciences, Universiti Malaysia Pahang, Lebuhraya Tun Razak, Gambang 26300, Pahang, Malaysia; rahmanmohd@ump.edu.my
[3] Institute for Mathematical Research, Universiti Putra Malaysia, Serdang 43400, Selangor, Malaysia; norihana@upm.edu.my
[4] Department of Mathematics, Faculty of Science, Universiti Putra Malaysia, Serdang 43400, Selangor, Malaysia
[5] Department of Mathematics, Babeş-Bolyai University, 400084 Cluj-Napoca, Romania; popm.ioan@yahoo.co.uk
* Correspondence: najiyah@utem.edu.my

Abstract: The flow of fluids over the boundaries of a rotating disc has many practical uses, including boundary-layer control and separation. Therefore, the aim of this study is to discuss the impact of unsteady magnetohydrodynamics (MHD) hybrid ferrofluid flow over a stretching/shrinking rotating disk. The time-dependent mathematical model is transformed into a set of ordinary differential equations (ODE's) by using similarity variables. The bvp4c method in the MATLAB platform is utilised in order to solve the present model. Since the occurrence of more than one solution is presentable, an analysis of solution stabilities is conducted. Both solutions were surprisingly found to be stable. Meanwhile, the skin friction coefficient, heat transfer rate—in cooperation with velocity— and temperature profile distributions are examined for the progressing parameters. The findings reveal that the unsteadiness parameter causes the boundary layer thickness of the velocity and temperature distribution profile to decrease. A higher value of magnetic and mass flux parameter lowers the skin friction coefficient. In contrast, the addition of the unsteadiness parameter yields a supportive effect on the heat transfer rate. An increment of the magnetic parameter up to 30% reduces the skin friction coefficient by 15.98% and enhances the heat transfer rate approximately up to 1.88%, significantly. In contrast, the heat transfer is rapidly enhanced by improving the mass flux parameter by almost 20%.

Keywords: hybrid ferrofluid; magnetohydrodynamics; rotating disk; stability analysis; unsteady flow

MSC: 76D10; 76M55; 34B15

1. Introduction

Convective transport has had a noteworthy impact io many real applications such as energy-producing plants, energy distribution systems, and environmental problems [1]. The convective transport can be induced by diffusion and advection where the diffusion refers to the random Brownian motion, whereas the advection refers to the transportation of heat by a larger-scale motion. Due to the substance of its theory and concepts, the ideas of convective transport have been extended to many fluid models that cover Newtonian and non-Newtonian fluid types. Additionally, the model of Eyring Powell fluid has been investigated by Al Jabali et al. [2] and Khalil et al. [3], whereas the Jeffrey model was considered by Shehzad et al. [4] and Kasim et al. [5]. Other interesting models such as viscoelastic can be found in Kasim et al. [6]. Additional previously studied models include

the viscous model [7], Casson model [8], and micropolar model [9]. The development of the fluid flow modelling is continued with the discovery of the upgraded thermal fluid. In the late 20th century, nanofluids were introduced in an effort to host the concept of the diffusion of nanoscale particles into fluids. The presence of nanofluids has been shown to increase the capacity for thermal conductivity. A pioneering study on nanofluids was conducted by Choi and Eastman [10]. Since then, this field of research has continued to receive high attention from researchers both experimentally and theoretically. This situation can be seen from the increase in publications every year where the contribution is based on the analysis of the fluid characteristics induced by the different geometries such as rectangular enclosure [11–13], stretching/shrinking sheet [14–17], thin needle [18,19], rotating disk [20], asymmetric wavy channel [21], vertical plate [22], and moving inclined [23]. These investigations also involve several significant effects including chemical reactions, magnetic fields, viscous dissipation circumstance, Dufour and Soret consequence, activation energy, and Joule heating. Simulations investigating the convective transport and heat transfer in cryogenic fuel tanks have been documented in refs. [24,25] where the improved algorithms determining the output were proposed. The analysis of heat transfer characteristics in a thermal energy storage system using single and multi-phase cooled heat sinks is presented in Alireza [26] where the evolution of the experimental, numerical, and computational efforts on energy storage was presented in detail.

The hybrid nanofluid offers a higher heat transfer rate in comparison to conventional nanofluid. This fluid is widely used in several applications and mainly can be found in heat exchangers activities, vehicle brake systems, solar industries, and also in refrigerator production [27]. The earlier studies which applied the hybrid nanoparticles in their investigations were Turcu et al. [28] and Jana et al. [29]. The composition of Cu-Al_2O_3/water was successfully studied by Suresh et al. [30] in discovering fluid with good thermal conductivity. The input stated, that despite having low thermal conductivity, Al_2O_3 offers a good chemical motionlessness in alumina which compromises a stable composition. A further study on combining Al_2O_3 with supplementary nanoparticles was established by Singh and Sarkar [31], Farhana et al. [32], and Takabi and Salehi [33]. Some other interesting publications on the development of the theoretical study of hybrid nanofluid can be viewed in refs. [34–42] where the investigations were performed using different particles, approaches, and various surfaces. Furthermore, some other publications reviewing the progress of hybrid nanofluids are documented in refs. [43–46].

Taking advantage of the progress of nanotechnology, scientists first created ferrofluid to counter the problem of logistics of bringing rocket fuel. The idea of this innovation is based on how to direct the fluid in space, and it is supported by the concept of the magnetic fluid can be well-ordered by a magnetic field. Then, the liquid fuel is mixed with the ferrofluid in the system together with the external magnetic field. The liquid with particles of Fe_3O_4 in nanometres size that happened in conventional base fluids is referred to as ferro-nanofluids or sometimes it is just called ferrofluid. Similar to nanofluids, ferrofluid also has high thermal conductivities and a great heat transfer rate, which is very important in device production. In fact, this technological fluid can be found in the production of hard drives where it is used to seal the interior of devices in order to avoid dust or external source damage to the delicate plate.

Due to the importance and many applications, interest in investigating ferrofluid came into demand for both experimental and simulated procedures. Khan et al. [47] provided a solution for heat transfer analysis of ferrofluid in the presence of viscous dissipation and concluded that kerosene-based ferrofluids developed high skin friction and Nusselt numbers compared to water-based ferrofluids. The investigation of ferrofluid, later on, was extended by other researchers by considering different surfaces. For instance, Qasim et al. [48] consider the stretching cylinder as the surface where the fluid is moving while Mehrez and Cafsi [49] proposed the flow in a rectangular channel. Further research on the topic of ferrofluid has been proposed by Sekar and Raju [50] and Hamid et al. [51] where the ferrofluid is considered together with dust particles and was studied as a two-

phase flow. Goshayeshi et al. [52] considered the effect of particle size and types in their investigation while Rashad [53] investigated the anisotropic impact on the flow field. In the same year, the same author documented the analysis of ferrofluid under thermal radiation and MHD circumstances [54]. The demand for investigating ferrofluid led to the development of new ideas and this progress is detailed out in refs. [55–61].

The interest in innovating the effective fluid has led to the discovery of hybrid ferrofluids where the investigations have involved multiple nanoparticles scattered in ferrofluid. Chu et al. [62] provided a solution for hybrid ferrofluids along with multi-wall carbon nanotubes (MWCNT) in a cavity for natural convection by applying a finite element scheme. It is revealed that the hybridization of ferrite nanoparticles uplifts in a physical thermos to see the studied flow. In the same year, Kumar et al. [63] proposed an investigation under the topic of MHD hybrid ferrofluid together with the effect of irregular heat source/sink towards the flow of the radiative thin film. The output declared from the hybrid ferrofluid intensifies the heat transfer rate in comparison with the conventional ferrofluid. A very recent study on this topic was presented by Anuar et al. [64] where their study of hybrid ferrofluid ($CoFe_2O_4$–Fe_3O_4/water) was focused on exponentially deformable sheets in stagnation point region. Apart from these mentioned studies, other interesting reports on hybrid ferrofluids can be found in refs. [65–67]. One real application that can be highlighted from the uses of hybrid ferrofluids is that it can be used as seeds for acid mine drainage (AMD) treatment. The use of a hybrid ferrofluid will provide a sustainable remedy for wastewater treatment, especially for AMD since the presence of AMD will cause severe destruction to the environment and predominantly disturb human life, aquatic organisms, animals, and also plants. The special properties of hybrid ferrofluids are unique magnetized characteristics with additional low toxicity and strong capacity for contaminant removal, which have led to enhancing the chemical reactivities [68].

As mentioned previously, the study on fluid flow normally deviates from its geometries. The pioneering study on infinite rotating disk was performed by Von Kármán [69] where the flow is taken as a viscous flow in which the disk rotates through uniform angular velocity. The Navier–Stokes equations representing the mathematical model are reduced to ordinary differential equations by adopting the similarity variables. The ideas from Von Kármán's work have been extended by Fang [70] where the investigation was focused on the flow over the stretchable rotating disk and later Fang and Zhang [71] extend to two infinite stretchable disks. Turkyilmazoglu [72] considered the presence of a magnetic field together with viscous dissipation and joule heating in the investigation after considering the unsteady flow over a rotating disk with outer radial flow [73]. The unsteady flow over a decelerating rotating sphere was then established by Turkyilmazoglu [74]. Another analysis of flow over a rotating disk was documented in refs. [75–78]. The study of flow over a rotating disk is still in demand due to its available applications in industries and engineering activities such as the viscometers instrument, turbines industries, rotating disk electrodes, mechanical devices, and Brake rotors [79,80].

Motivated by the studies available in the literature and fulfilling the gap in the study of hybrid ferrofluids, this study discusses the investigation on the unsteady flow of hybrid ferrofluid flow over a rotating disk. It is worth mentioning that the non-unique solutions are available but are restricted to pertinent parameters and the stability analysis affirms the physical solution.

2. Mathematical Formulation

Consider the unsteady flow of hybrid ferrofluids with different base fluids (Fe_3O_4-$CoFe_2O_4$/H_2O-EG and Fe_3O_4-$CoFe_2O_4$/H_2O) induced by a rotating disk as illustrated in Figure 1 with the imposition of suction/injection effect. The disk rotates with the velocity, $v = v_w$ while being stretched/shrunk with velocity, $u = u_w$. Moreover, it is considered that the suction/injection effect is embedded with the mass flux velocity, $w = w_w$. The constant surface and ambient temperatures are symbolized as T_w and T_∞, respectively. A further assumption is that the magnetic field is applied normally to the disk such that

$B^* = B_0/\sqrt{1-ct}$ with constant magnetic strength B_0 (see Appendix A for the derivation of magnetic field).
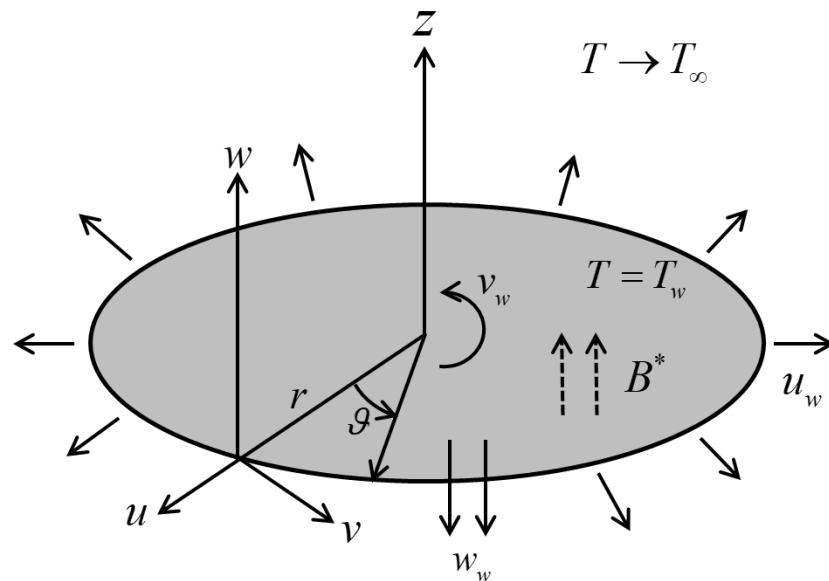

Figure 1. The flow configuration of the fluid.

Thus, the governing equations in cylindrical coordinates $(r, \vartheta, 0)$ are [77,80,81]:

$$\frac{\partial}{\partial r}(ru) + \frac{\partial}{\partial z}(rw) = 0,\tag{1}$$

$$\frac{\partial u}{\partial t} + u\frac{\partial u}{\partial r} + w\frac{\partial u}{\partial r} - \frac{v^2}{r} = -\frac{1}{\rho_{hnf}}\frac{\partial p}{\partial r} + \frac{\mu_{hnf}}{\rho_{hnf}}\left(\frac{\partial^2 u}{\partial r^2} + \frac{1}{r}\frac{\partial u}{\partial r} + \frac{\partial^2 u}{\partial z^2} - \frac{u}{r^2}\right) - \frac{\sigma_{hnf}}{\rho_{hnf}}B^{*2}u,\tag{2}$$

$$\frac{\partial v}{\partial t} + u\frac{\partial v}{\partial r} + w\frac{\partial v}{\partial z} + \frac{uv}{r} = \frac{\mu_{hnf}}{\rho_{hnf}}\left(\frac{\partial^2 v}{\partial r^2} + \frac{1}{r}\frac{\partial v}{\partial r} + \frac{\partial^2 v}{\partial z^2} - \frac{v}{r^2}\right) - \frac{\sigma_{hnf}}{\rho_{hnf}}B^{*2}v,\tag{3}$$

$$\frac{\partial w}{\partial t} + u\frac{\partial w}{\partial r} + w\frac{\partial w}{\partial z} = -\frac{1}{\rho_{hnf}}\frac{\partial p}{\partial z} + \frac{\mu_{hnf}}{\rho_{hnf}}\left(\frac{\partial^2 w}{\partial r^2} + \frac{1}{r}\frac{\partial w}{\partial r} + \frac{\partial^2 w}{\partial z^2}\right),\tag{4}$$

$$\frac{\partial T}{\partial t} + u\frac{\partial T}{\partial r} + w\frac{\partial T}{\partial z} = \frac{k_{hnf}}{(\rho C_p)_{hnf}}\left(\frac{\partial^2 T}{\partial r^2} + \frac{1}{r}\frac{\partial T}{\partial r} + \frac{\partial^2 T}{\partial z^2}\right),\tag{5}$$

subject to:

$$u = \lambda u_w, \quad v = v_w, \quad w = w_w, \quad T = T_w \quad \text{at} \quad z = 0\tag{6}$$

$$u \to 0, \quad v \to 0, \quad w \to 0, \quad T \to T_\infty \quad \text{as} \quad z \to \infty\tag{7}$$

where (u, v, w) are the velocities for $(r, \vartheta, 0)$ directions while T is the temperature. It is further assumed that $u_w = \Omega r/(1-ct)$, $v_w = \Omega r/(1-ct)$ where t and Ω are the respective time and angular velocity (constant), accordingly. Furthermore, c represents the unsteadiness strength (constant) while $w_w = -w_0/\sqrt{1-ct}$ is the mass velocity with constant w_0. Moreover, $\lambda = 0$ represents a static disk while $\lambda > 0, \lambda < 0$ stand for the stretching/shrinking disk, respectively.

The thermophysical properties of the base fluids (water and water–ethylene glycol), magnetite, and cobalt ferrite nanoparticles are described in Table 1 [66]. Meanwhile, the correlations for hybrid nanofluid are shown in Table 2 [33].

Table 1. Physical properties of the respective base fluid and nanoparticles.

Properties	Base Fluid		Nanoparticles	
	Water	Water–Ethylene Glycol	Magnetite	Cobalt Ferrite
ρ (kg/m^3)	997.1	1057	5180	4908
C_p (J/kgK)	4179	3287	670	700
k (W/mK)	0.613	0.424	9.8	3.6
σ (S/m)	0.05	0.005	0.74×10^6	1.1×10^7
Prandtl number, (Pr)	6.2	30	-	-

Table 2. Thermophysical properties of hybrid nanofluid.

Thermophysical Properties	Correlations
Thermal conductivity	$\dfrac{k_{hnf}}{k_f} = \dfrac{\frac{\varphi_1 k_{n1} + \varphi_2 k_{n2}}{\varphi_{hnf}} + 2k_f + 2(\varphi_1 k_{n1} + \varphi_2 k_{n2}) - 2\varphi_{hnf} k_f}{\frac{\varphi_1 k_{n1} + \varphi_2 k_{n2}}{\varphi_{hnf}} + 2k_f - (\varphi_1 k_{n1} + \varphi_2 k_{n2}) + \varphi_{hnf} k_f}$
Electrical conductivity	$\dfrac{\sigma_{hnf}}{\sigma_f} = \dfrac{\frac{\varphi_1 \sigma_{n1} + \varphi_2 \sigma_{n2}}{\varphi_{hnf}} + 2\sigma_f + 2(\varphi_1 \sigma_{n1} + \varphi_2 \sigma_{n2}) - 2\varphi_{hnf} \sigma_f}{\frac{\varphi_1 \sigma_{n1} + \varphi_2 \sigma_{n2}}{\varphi_{hnf}} + 2\sigma_f - (\varphi_1 \sigma_{n1} + \varphi_2 \sigma_{n2}) + \varphi_{hnf} \sigma_f}$
Heat capacity	$(\rho C_p)_{hnf} = \left(1 - \varphi_{hnf}\right)(\rho C_p)_f + \varphi_1 (\rho C_p)_{n1} + \varphi_2 (\rho C_p)_{n2}$
Density	$\rho_{hnf} = \left(1 - \varphi_{hnf}\right)\rho_f + \varphi_1 \rho_{n1} + \varphi_2 \rho_{n2}$
Dynamic viscosity	$\mu_{hnf} = \dfrac{\mu_f}{\left(1 - \varphi_{hnf}\right)^{2.5}}$

Now, consider the following similarity transformations [77,80,81]:

$$u = \frac{\Omega r}{1 - ct} f'(\eta), v = \frac{\Omega r}{1 - ct} g(\eta), w = -\frac{2\sqrt{\Omega \nu_f}}{\sqrt{1 - ct}} f(\eta), \theta(\eta) = \frac{T - T_\infty}{T_w - T_\infty}, \eta = \sqrt{\frac{\Omega}{\nu_f}} \frac{z}{\sqrt{1 - ct}}. \tag{8}$$

Equation (1) is fully satisfied by considering the similarity variables in Equation (8). Furthermore, the reduced Equations (2)–(5) are:

$$\frac{\mu_{hnf}/\mu_f}{\rho_{hnf}/\rho_f} f''' + 2ff'' - f'^2 + g^2 - S\left(f' + \frac{1}{2}\eta f''\right) - \frac{\sigma_{hnf}/\sigma_f}{\rho_{hnf}/\rho_f} M f' = 0, \tag{9}$$

$$\frac{\mu_{hnf}/\mu_f}{\rho_{hnf}/\rho_f} g'' + 2fg' - 2f'g - S\left(g + \frac{1}{2}\eta g'\right) - \frac{\sigma_{hnf}/\sigma_f}{\rho_{hnf}/\rho_f} M g = 0, \tag{10}$$

$$\frac{1}{\text{Pr}} \frac{k_{hnf}/k_f}{(\rho C_p)_{hnf}/(\rho C_p)_f} \theta'' + 2f\theta' - \frac{1}{2}S\eta \theta' = 0, \tag{11}$$

subject to:

$$f(0) = \frac{B}{2}, \quad f'(0) = \lambda, \quad g(0) = 1, \quad \theta(0) = 1, \tag{12}$$

$$f'(\eta) \to 0, \quad g(\eta) \to 0, \quad \theta(\eta) \to 0, \quad \text{as} \quad \eta \to \infty \tag{13}$$

The parameters relevant to this problem are the unsteadiness parameter $S = c/\Omega$, Prandtl number $\text{Pr} = (\mu C_p)_f / k_f$, suction/injection parameter $B = w_0 / \sqrt{\Omega \nu_f}$, and magnetic parameter $M = B_0^2 \sigma_f / \rho_f \Omega$. Meanwhile, the skin friction coefficients are C_f (radial direction) and C_g (azimuthal direction), and the local Nusselt number for evaluating heat transfer performance is Nu_r (see Waini et al. [81]):

$$C_f = \frac{\mu_{hnf}}{\rho_f u_w^2} \left(\frac{\partial u}{\partial z}\right)_{z=0}, C_g = \frac{\mu_{hnf}}{\rho_f v_w^2} \left(\frac{\partial v}{\partial z}\right)_{z=0}, Nu_r = -\frac{r k_{hnf}}{k_f (T_w - T_\infty)} \left(\frac{\partial T}{\partial z}\right)_{z=0} \tag{14}$$

Using Equations (8) and (13), one obtains (see Waini et al. [81]):

$$\text{Re}_r^{1/2} C_f = \frac{\mu_{hnf}}{\mu_f} f''(0), \ \text{Re}_r^{1/2} C_g = \frac{\mu_{hnf}}{\mu_f} g'(0), \ \text{Re}_r^{-1/2} Nu_r = -\frac{k_{hnf}}{k_f} \theta'(0), \tag{15}$$

where $\text{Re}_r = u_w r / \nu_f$ is the local Reynolds number.

3. Stability Analysis

The dual solutions are examined to test their stability by employing stability analysis [82,83]. Firstly, consider the following variables:

$$u = \frac{\Omega r}{1-ct} \frac{\partial f}{\partial \eta}(\eta, \tau), v = \frac{\Omega r}{1-ct} g(\eta, \tau), w = -\frac{2\sqrt{\Omega \nu_f}}{\sqrt{1-ct}} f(\eta, \tau), \theta(\eta, \tau) = \frac{T-T_\infty}{T_w-T_\infty},$$
$$\eta = \sqrt{\frac{\Omega}{\nu_f}} \frac{z}{\sqrt{1-ct}}, \tau = \frac{\Omega r}{1-ct} t \tag{16}$$

where τ is the time variable. Substituting Equation (16) into Equations (2)–(5),

$$\frac{\mu_{hnf}/\mu_f}{\rho_{hnf}/\rho_f} \frac{\partial^3 f}{\partial \eta^3} + 2f \frac{\partial^2 f}{\partial \eta^2} - \left(\frac{\partial f}{\partial \eta}\right)^2 + g^2 - S\left(\frac{\partial f}{\partial \eta} + \frac{1}{2}\eta\frac{\partial^2 f}{\partial \eta^2}\right) - (1+S\tau)\frac{\partial^2 f}{\partial \eta \partial \tau} - \frac{\sigma_{hnf}/\sigma_f}{\rho_{hnf}/\rho_f} M\frac{\partial f}{\partial \eta} = 0, \tag{17}$$

$$\frac{\mu_{hnf}/\mu_f}{\rho_{hnf}/\rho_f} \frac{\partial^2 g}{\partial \eta^2} + 2f \frac{\partial g}{\partial \eta} - 2\frac{\partial f}{\partial \eta} g - S\left(g + \frac{1}{2}\eta\frac{\partial g}{\partial \eta}\right) - (1+S\tau)\frac{\partial^2 g}{\partial \eta \partial \tau} - \frac{\sigma_{hnf}/\sigma_f}{\rho_{hnf}/\rho_f} Mg = 0, \tag{18}$$

$$\frac{1}{\text{Pr}} \frac{k_{hnf}/k_f}{(\rho C_p)_{hnf}/(\rho C_p)_f} \frac{\partial^2 \theta}{\partial \eta^2} + 2f \frac{\partial \theta}{\partial \eta} - \frac{1}{2}S\eta\frac{\partial \theta}{\partial \eta} - (1+S\tau)\frac{\partial \theta}{\partial \tau} = 0, \tag{19}$$

subject to:

$$f(0, \tau) = \frac{B}{2}, \quad \frac{\partial f}{\partial \eta}(0, \tau) = \lambda, \quad g(0, \tau) = 1, \quad \theta(0, \tau) = 1, \tag{20}$$

$$\frac{\partial f}{\partial \eta}(\eta, \tau) \to 0, \quad g(\eta, \tau) \to 0, \quad \theta(\eta, \tau) \to 0 \quad \text{as} \quad \eta \to \infty \tag{21}$$

The perturbation function as suggested by early reference is [83]:

$$\begin{aligned} f(\eta, \tau) &= f_0(\eta) + e^{-\alpha\tau} F(\eta, \tau), \\ g(\eta, \tau) &= g_0(\eta) + e^{-\alpha\tau} G(\eta, \tau), \\ \theta(\eta, \tau) &= \theta_0(\eta) + e^{-\alpha\tau} H(\eta, \tau) \end{aligned} \tag{22}$$

where $F(\eta, \tau)$, $G(\eta, \tau)$, and $H(\eta, \tau)$ are arbitrary functions and relatively smaller than $f_0(\eta)$, $g_0(\eta)$, and $\theta_0(\eta)$, while α is the corresponding eigenvalue. Equation (22) is applied into Equations (17)–(21) and by setting $\tau = 0$, $F(\eta, \tau) = F_0(\eta)$, $G(\eta, \tau) = G_0(\eta)$, and $H(\eta, \tau) = H_0(\eta)$, the linearized equations are

$$\frac{\mu_{hnf}/\mu_f}{\rho_{hnf}/\rho_f} F_0''' + 2(f_0 F_0'' + f_0'' F_0) - 2f_0' F_0' + 2g_0 G_0 - S\left(F_0' + \frac{1}{2}\eta F_0''\right) + \alpha F_0' - \frac{\sigma_{hnf}/\sigma_f}{\rho_{hnf}/\rho_f} M F_0' = 0, \tag{23}$$

$$\frac{\mu_{hnf}/\mu_f}{\rho_{hnf}/\rho_f} G_0'' + 2(f_0 G_0' + g_0' F_0) - 2(f_0' G_0 + g_0 F_0') - S\left(G_0 + \frac{1}{2}\eta G_0'\right) + \alpha G_0 - \frac{\sigma_{hnf}/\sigma_f}{\rho_{hnf}/\rho_f} M G_0 = 0, \tag{24}$$

$$\frac{1}{\text{Pr}} \frac{k_{hnf}/k_f}{(\rho C_p)_{hnf}/(\rho C_p)_f} H_0'' + 2(f_0 H_0' + \theta_0' F_0) - \frac{1}{2}S\eta H' + \alpha H_0 = 0 \tag{25}$$

subject to:

$$F_0(0) = 0, \quad F_0'(0) = 0, \quad G_0(0) = 0, \quad H_0(0) = 0, \tag{26}$$

$$F_0'(\eta) \to 0, \quad G_0(\eta) \to 0, \quad H_0(\eta) \to 0 \quad \text{as} \quad \eta \to \infty. \tag{27}$$

The set of eigenvalues α are obtained from Equations (23)–(25) if $F_0'(\eta) \to 0$ as $\eta \to \infty$ in Equation (27) is replaced by $F''(0) = 1$ [84].

4. Results and Discussion

Discussions of the obtained results are provided in this section. The bvp4c solver was used for the computation. This solver occupies a finite difference method that employs the three-stage Lobatto IIIa formula, see Shampine et al. [85,86]. The present results were validated by conducting a comparison with previously published data. In this respect, Table 3 provides the validation of test values when $\varphi_{hnf} = B = M = 0$ with different values of S, and an excellent agreement can be observed from the comparison. Therefore, the present results are acceptable and accurate.

Table 3. Validation of numerical values when $\varphi_{hnf} = B = M = 0$ and different S.

S	Present		Fang and Tao [77]		Waini et al. [81]	
	$f''(0)$	$g'(0)$	$f''(0)$	$g'(0)$	$f''(0)$	$g'(0)$
-1	0.719787	-0.236575	0.7198	-0.2366	0.719787	-0.236575
-2	0.931507	0.154981	0.9315	0.1550	0.931507	0.154981
-5	1.562797	1.360850	1.5627	1.3609	1.562797	1.360850
-10	2.600801	3.413860	2.6008	3.4139	2.600801	3.413860

Furthermore, the total composition of Al_2O_3 and Cu concentrations in this study are considered as 1% of Fe_3O_4 ($\varphi_1 = 1\%$) and 1% of $CoFe_2O_4$ ($\varphi_2 = 1\%$). The Prandtl number subject to the water base fluid is $Pr = 6.2$ and $Pr = 30$ for water–ethylene glycol. The dual solution's availability is possible, as displayed in Figures 2–13 when the parameters are used within the allocated interval; unsteadiness decelerating parameter $-1.2 \leq S \leq -1$, magnetic parameter $0 \leq M \leq 0.2$, suction/injection parameter $-0.2 \leq B \leq 0.2$ while other parameters are fixed such that $\phi_1, \phi_2 = 1\%$ $\left(\phi_{hnf} = 2\%\right)$ and $\lambda = 0$.
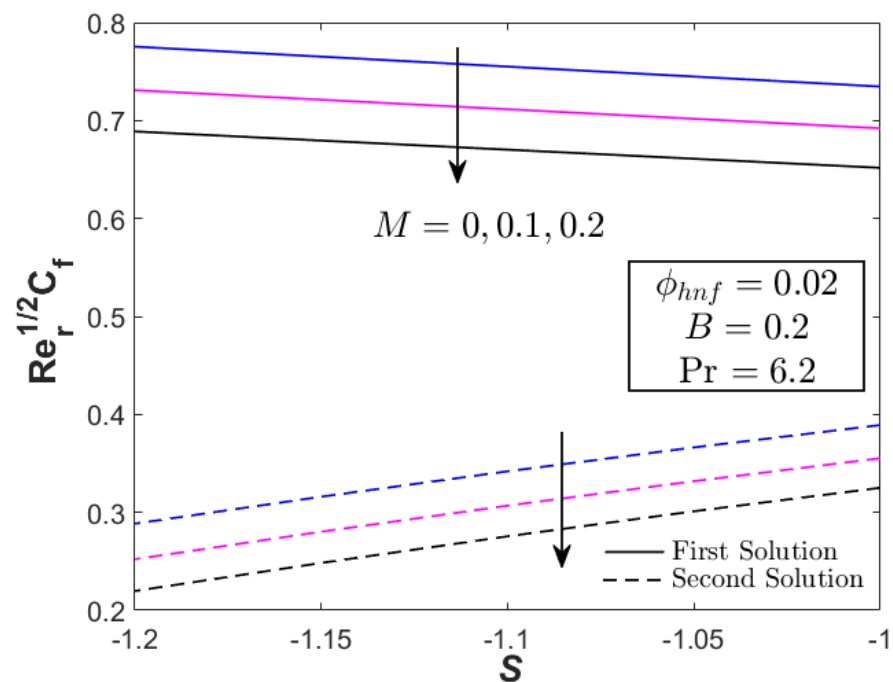

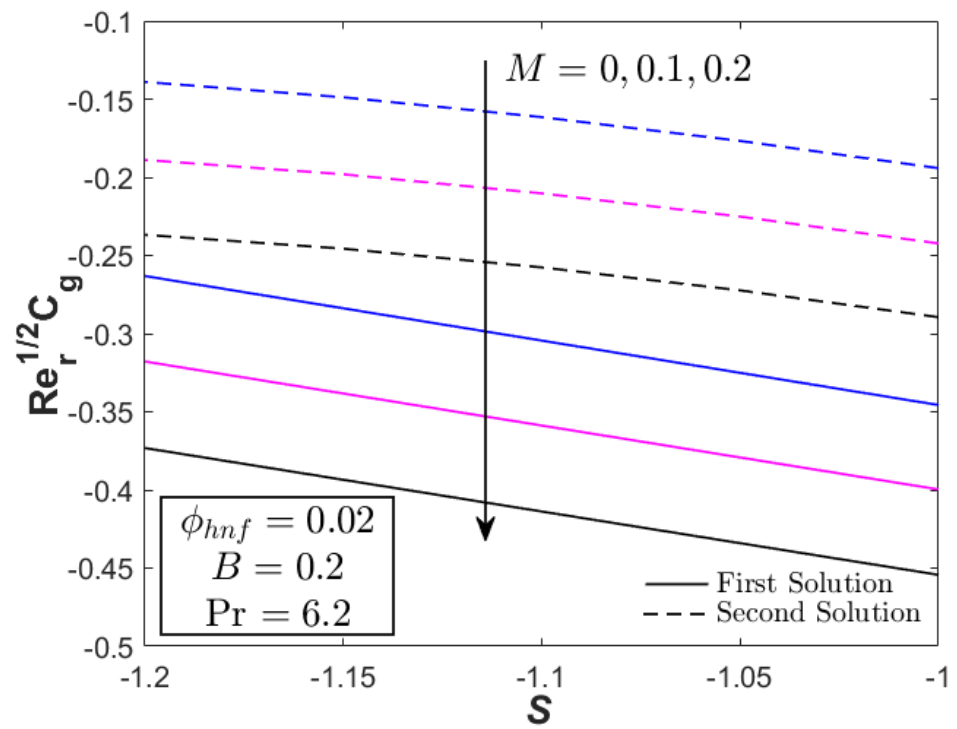**Figure 2.** $Re_r^{1/2}C_f$ (radial direction) towards S for several M.

Figure 3. $\mathrm{Re}_r^{1/2}C_g$ (azimuthal direction) towards S for several M.
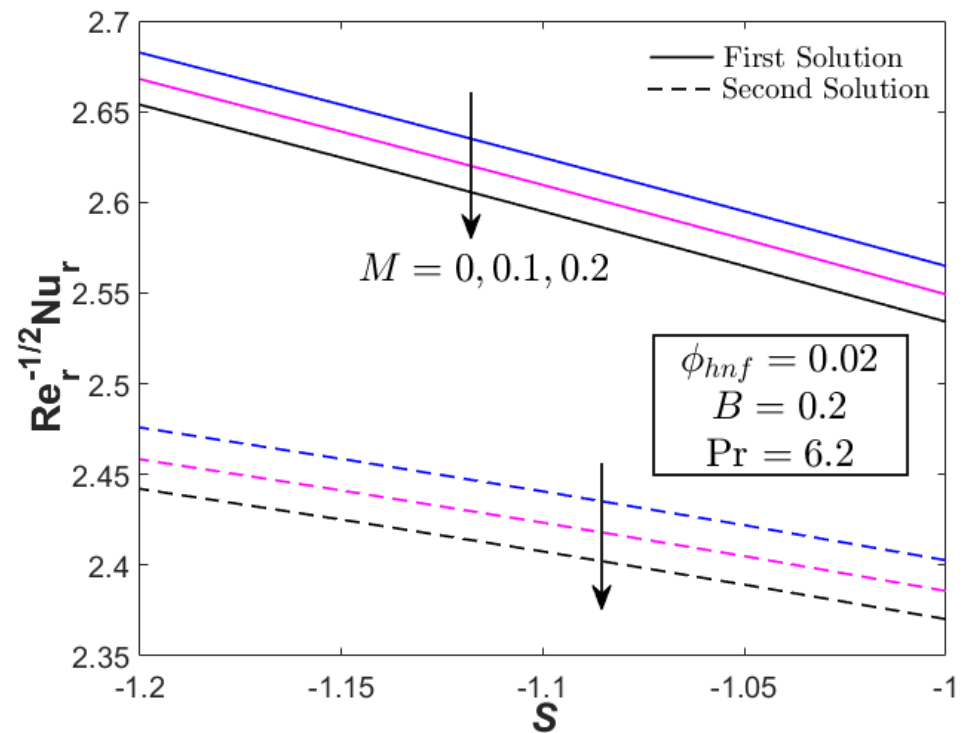

Figure 4. $\mathrm{Re}_r^{-1/2}Nu_r$ towards S for several M.
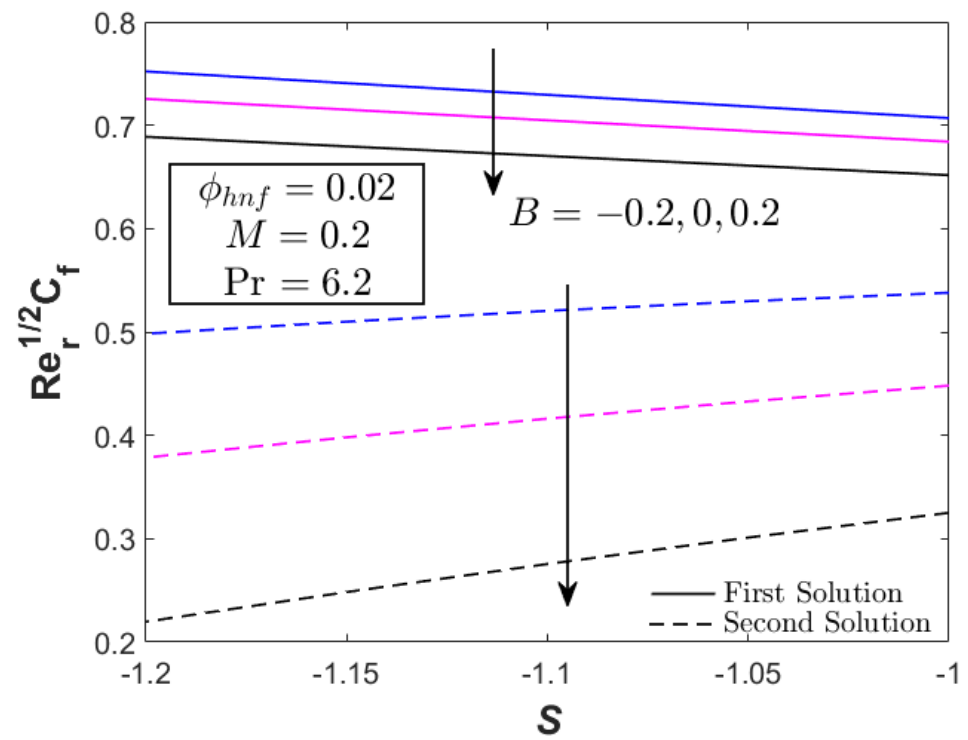
Figure 5. $\mathrm{Re}_r^{1/2}C_f$ (radial direction) towards S for several B.
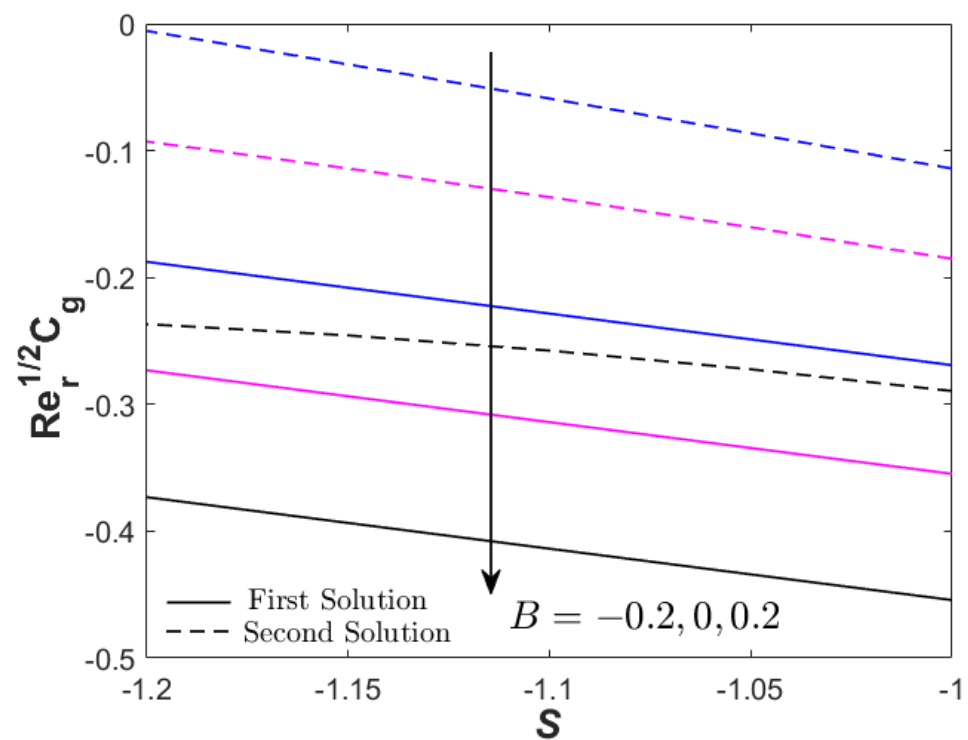
Figure 6. $\mathrm{Re}_r^{1/2}C_g$ (azimuthal direction) towards S for several B.
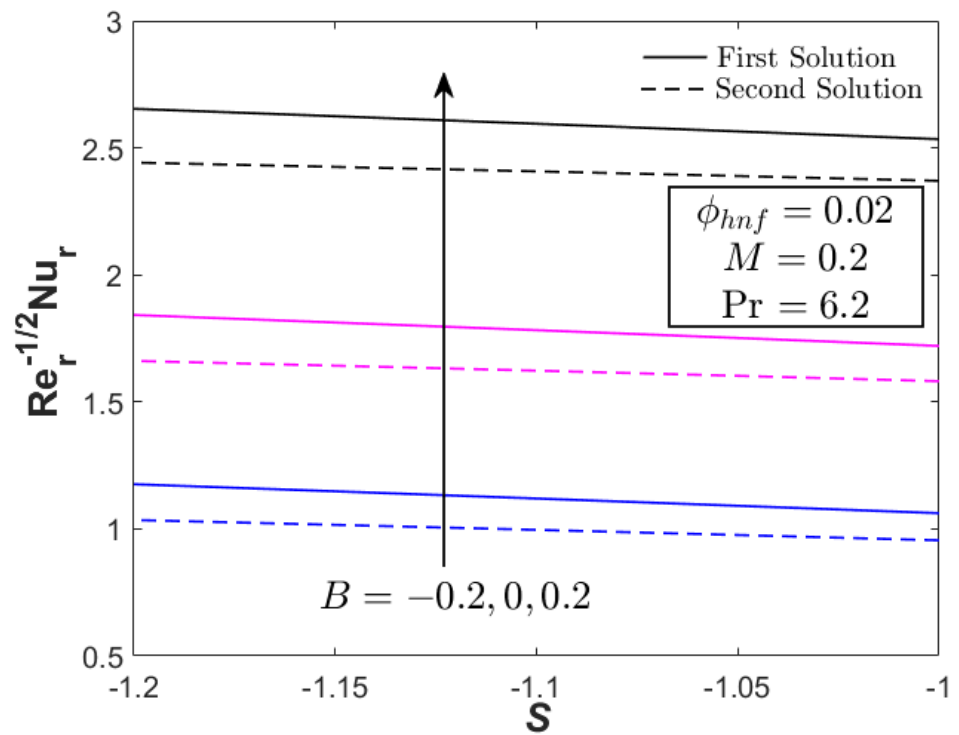
Figure 7. $\mathrm{Re}_r^{-1/2}Nu_r$ towards S for several B.
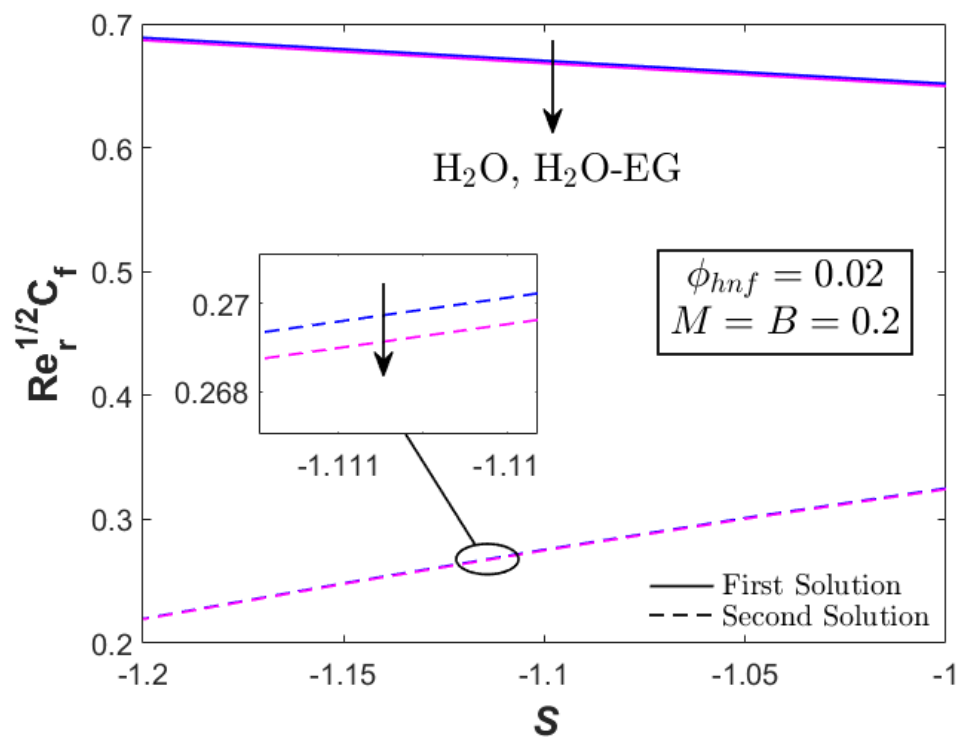

Figure 8. $\mathrm{Re}_r^{1/2}C_f$ (radial direction) towards S for different base fluid.
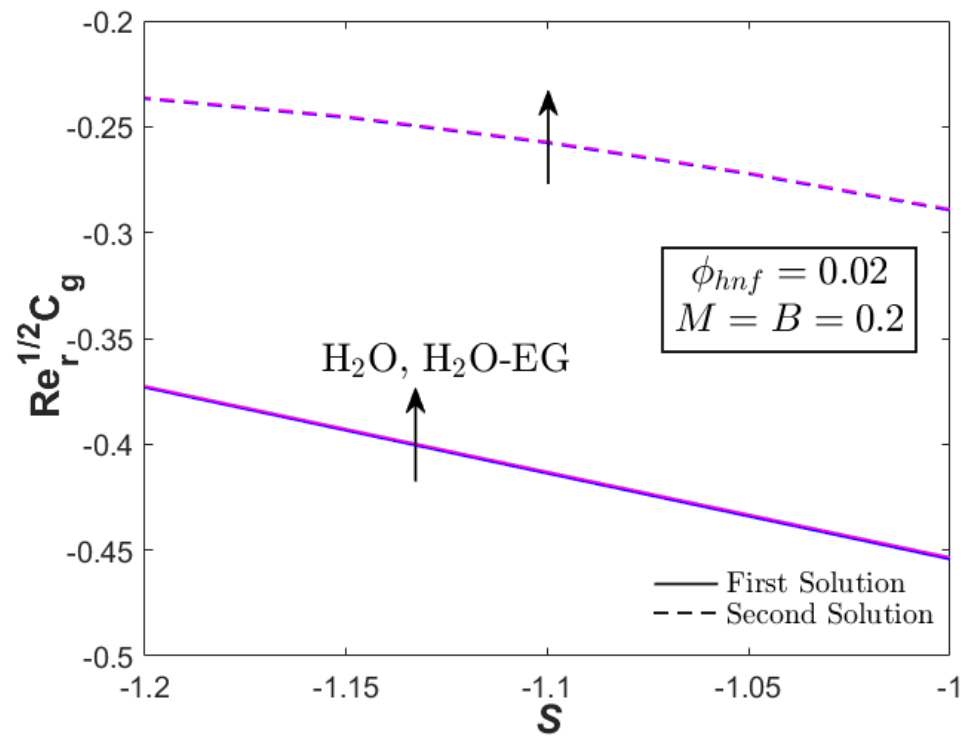
Figure 9. $\text{Re}_r^{1/2} C_g$ (azimuthal direction) towards S for different base fluid.
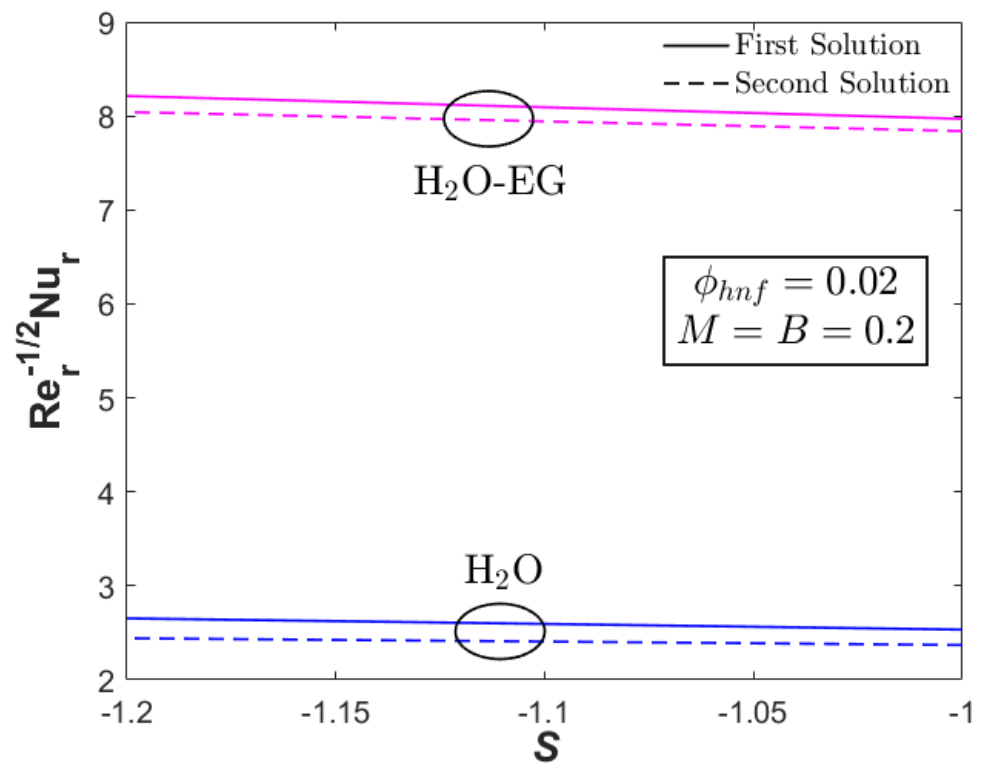
Figure 10. $\text{Re}_r^{-1/2} Nu_r$ towards S for different base fluid.
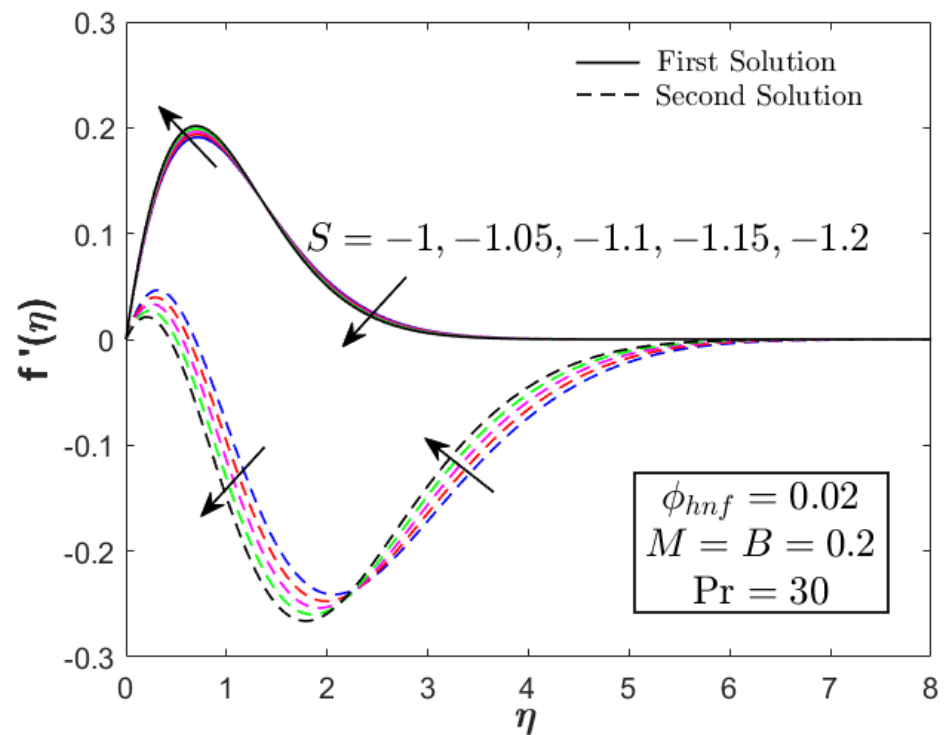
Figure 11. Radial velocity profile of Fe_3O_4-$CoFe_2O_4/H_2O$-EG for several S.
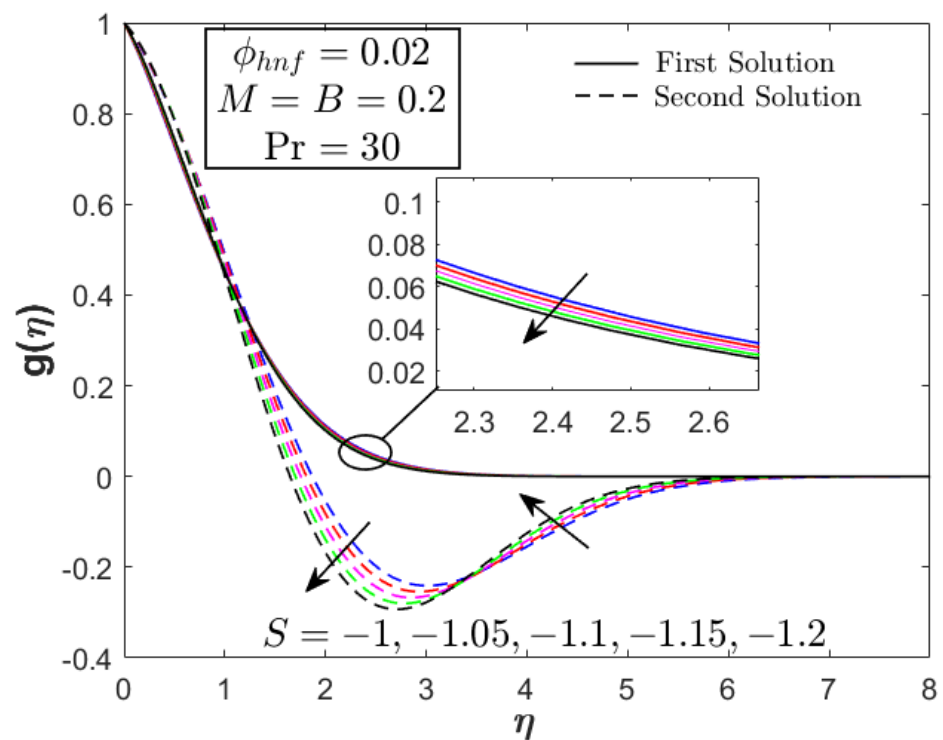
Figure 12. Azimuthal velocity profile of Fe_3O_4-$CoFe_2O_4/H_2O$-EG for several S.
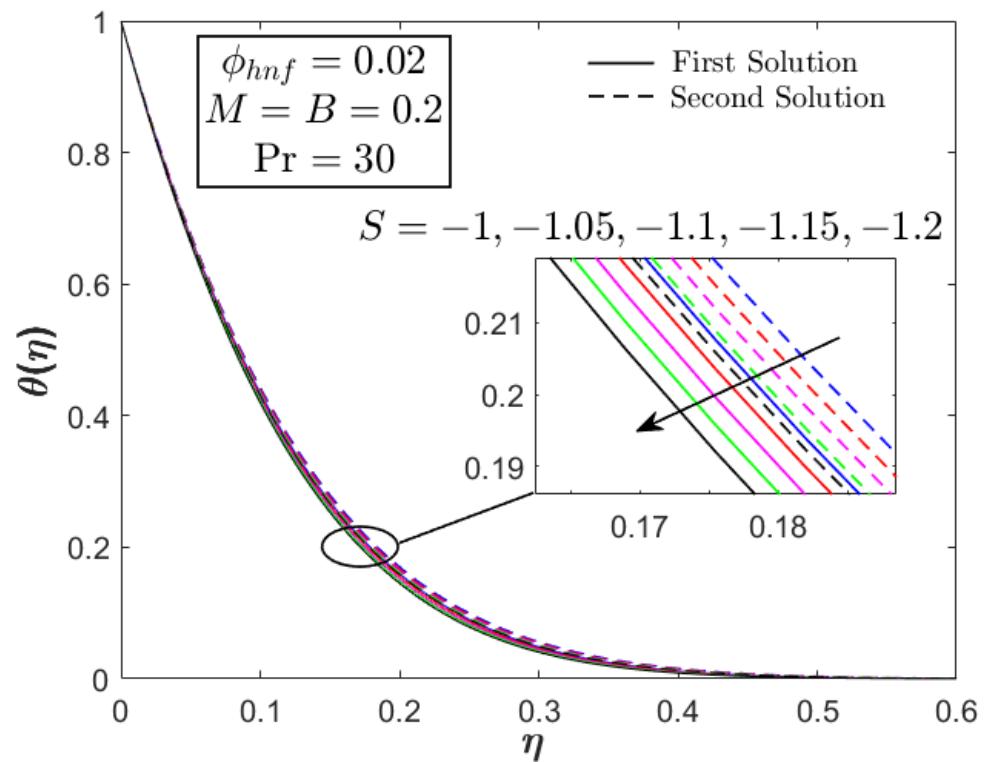
Figure 13. Temperature profile of Fe_3O_4-$CoFe_2O_4/H_2O$-EG for several S.

The new numerical results obtained from this present study are presented in Tables 4 and 5. Here, the values of the physical quantities such as $Re_r^{1/2}C_f$, $Re_r^{1/2}C_g$, and $Re_r^{-1/2}Nu_r$ are obtained for varied values of M with different base fluids (H_2O-EG and H_2O). For the first solution, the results show a decrement in these physical quantities as M increases. Quantitatively, a 15.98% decrement is observed for the values of $Re_r^{1/2}C_f$ when M increases up to 30% ($M = 0.3$). Meanwhile, the reduction in $Re_r^{1/2}C_g$ is prominent with a 61.66% decrement and the values of $Re_r^{-1/2}Nu_r$ decrease with 1.88%. However, a significant increment is observed for $Re_r^{-1/2}Nu_r$ when H_2O-EG is considered with 107.60% compared to H_2O as the base fluid. Furthermore, the numerical results provided could be important to other researchers for future reference. Interestingly, multiple solutions are obtained under certain circumstances. To determine a realistic or stable solution, Table 6 shows the smallest eigenvalues α that were obtained from the eigenvalue problems (see Section 3). Surprisingly, both solutions give positive values ($\alpha > 0$) that reveal the stability of both solutions and the possibility of another solution with a negative eigenvalue [81].

Table 4. Values of $Re_r^{1/2}C_f$, $Re_r^{1/2}C_g$, and $Re_r^{-1/2}Nu_r$ for Fe_3O_4-$CoFe_2O_4/H_2O$-EG when $\varphi_{hnf} = 2\%$, $B = 0$, $S = -1$ and different values of M.

M	**First Solution**			**Second Solution**		
	$Re_r^{1/2}C_f$	$Re_r^{1/2}C_g$	$Re_r^{-1/2}Nu_r$	$Re_r^{1/2}C_f$	$Re_r^{1/2}C_g$	$Re_r^{-1/2}Nu_r$
0	0.765534	−0.251611	3.604480	0.512769	−0.088499	3.452206
0.1	0.722637	−0.302647	3.581163	0.478139	−0.136966	3.430586
0.2	0.681833	−0.354398	3.558560	0.446589	−0.185258	3.410523
0.3	0.643206	−0.406753	3.536762	0.418191	−0.233521	3.392171

Table 5. Values of $\text{Re}_r^{1/2}C_f$, $\text{Re}_r^{1/2}C_g$, and $\text{Re}_r^{-1/2}Nu_r$ for Fe$_3$O$_4$-CoFe$_2$O$_4$/H$_2$O when $\varphi_{hnf} = 2\%$, $B = 0$, $S = -1$ and different values of M.

M	First Solution			Second Solution		
	$\text{Re}_r^{1/2}C_f$	$\text{Re}_r^{1/2}C_g$	$\text{Re}_r^{-1/2}Nu_r$	$\text{Re}_r^{1/2}C_f$	$\text{Re}_r^{1/2}C_g$	$\text{Re}_r^{-1/2}Nu_r$
0	0.767572	−0.252281	1.755377	0.514134	−0.088735	1.617641
0.1	0.724783	−0.303179	1.737683	0.479588	−0.137073	1.599005
0.2	0.684071	−0.354788	1.720410	0.448097	−0.185238	1.581450
0.3	0.645516	−0.406997	1.703642	0.419732	−0.233372	1.565181

Table 6. Smallest eigenvalues when $\varphi_{hnf} = 2\%$, $B = M = 0$, and various S for Fe$_3$O$_4$-CoFe$_2$O$_4$/H$_2$O-EG.

S	Smallest Eigenvalues	
	First Solution	Second Solution
−1.1	6.0014	0.7442
−1.2	6.7395	0.8547
−1.3	6.9401	1.0462

The effects of magnetic M and unsteadiness S parameters on the physical quantities ($\text{Re}_r^{1/2}C_f$, $\text{Re}_r^{1/2}C_g$, and $\text{Re}_r^{-1/2}Nu_r$) are elucidated in Figures 2–4. The declining behaviour is noticed when a larger M value is considered. However, the opposite trend is shown for stronger deceleration strength ($S < 0$). Physically, the Lorentz force is created when the magnetic field is imposed on the boundary layer, and it is intensified for stronger magnetic field strength. This force possesses the flow and increases the shear stress on the surface, and consequently increases the thermal rate. It should be noted that the outcomes of this study are contradicted by its physical phenomenon due to the interaction between the magnetic field and the unsteadiness of the flow. This observation is supported by a previous study, see Waini et al. [81], which stated that the unsteadiness condition creates an obstacle to the flow and thermal behaviour of the fluid.

Figures 5–7 displayed the values of $\text{Re}_r^{1/2}C_f$, $\text{Re}_r^{1/2}C_g$, and $\text{Re}_r^{-1/2}Nu_r$ for different values of B (mass flux parameter). The quantities of $\text{Re}_r^{1/2}C_f$, and $\text{Re}_r^{1/2}C_g$ are lower for $B = 0.2$ (suction case). Physically, the wall suction causes a higher drag force and torque on the revolving disk and thus raising the shear stress. However, the opposite observation was seen in this study (see Figures 5 and 6). This is due to the simultaneous effect of the physical parameter on the flow. However, the behaviour is contradicted for $\text{Re}_r^{-1/2}Nu_r$ where $B = 0.2$ (suction case) gives higher values of $\text{Re}_r^{-1/2}Nu_r$.

Figures 8–10 are provided in order to investigate the impact of the different base fluids (H$_2$O and H$_2$O-EG) on the flow and thermal behaviour. Here, H$_2$O-EG contributes to enhancing the values of $\text{Re}_r^{1/2}C_g$, and $\text{Re}_r^{-1/2}Nu_r$. Meanwhile, the values of $\text{Re}_r^{1/2}C_f$ decline. This observation can be explained from the values of their Prandtl number, Pr. Note that H$_2$O-EG has larger Pr, i.e., Pr = 30 if compared to H$_2$O (Pr = 6.2). Larger Pr means the convection process for the flow is dominant. As a result, fluid momentum, rather than fluid conduction, is the best way to transmit heat. Additionally, the velocity and the temperature profiles of Fe$_3$O$_4$-CoFe$_2$O$_4$/H$_2$O-EG for several S are given in Figures 11–13. The thickness of the respective boundary layers is lessened as S becomes smaller. This implies that the gradient of these profiles near the wall is increased for stronger deceleration strength ($S < 0$) and gives higher values of the shear stress and heat transfer on the wall, as reported in Figures 4–6.

5. Conclusions

In this numerical study, various effects of the controlling parameters in the unsteady MHD hybrid ferrofluid flow and heat transfer over a rotating stretching/shrinking disk are discussed. The physical properties of the fluid are affected by different values of the

magnetic parameter, unsteadiness parameter, and the mass flux parameter which generate an impact on the skin friction coefficient, heat transfer rate, velocity profile, and temperature field. It is perceived that velocity profile and temperature field distributions decrease when increasing the unsteadiness parameter. On the other hand, it is found that a highly oscillating magnetic field forces the particles to rotate slower than the ferrofluid; therefore, resulting in an increment of viscosity. Consequently, a deterioration in the flow speed is observed as the value of the magnetic parameter increases up to 30%, thus decreasing the skin friction coefficient by 15.98% and the heat transfer rate approximately up to 1.88%, significantly. In contrast, the heat transfer is enhanced rapidly by improving the mass flux parameter by almost 20%. Furthermore, the use of H_2O-EG improves the thermal efficiency of the system when compared to H_2O as the base fluid. Finally, depending on the analysis of solution stability, both solutions are surprisingly found to be stable.

Author Contributions: Conceptualization, I.W., N.S.K., N.M.A., and I.P.; methodology, I.W. and N.S.K.; validation, I.W. and N.S.K.; writing—original draft, I.W., N.S.K., A.R.M.K., N.A.Z., and K.B.H.; review and editing, A.R.M.K., N.A.Z., and K.B.H. All authors have read and agreed to the published version of the manuscript.

Conflicts of Interest: The authors declare no conflict of interest.

Nomenclature

B	suction/injection parameter
B^*	magnetic field strength
B_0	constant magnetic strength
c	unsteadiness strength (constant)
C_f	skin friction coefficient (radial direction)
C_g	skin friction coefficient (azimuthal direction)
C_p	specific heat at constant pressure (J kg^{-1}K^{-1})
(ρC_p)	heat capacitance of the fluid (J K^{-1}m^{-3})
k	fluid thermal conductivity (m W^{-1}K^{-1})
M	magnetic parameter
Nu_r	local Nusselt number
Pr	Prandtl number
S	unsteadiness parameter
Re$_r$	local Reynolds number
t	time (*s*)
T	fluid temperature (K)
T_∞	ambient temperature (K)
T_w	surface temperature (K)
u, v, w	velocity component in the $(r, \vartheta, 0)$ directions (m s^{-1})
u_w	velocity of the stretching/shrinking disk (m s^{-1})
v_w	velocity of the rotating disk (m s^{-1})
w_w	mass flux velocity (m s^{-1})
w_0	constant
$(r, \vartheta, 0)$	cylindrical coordinates (m)

Greek symbols

α	eigenvalue
λ	velocity ratio parameter
τ	dimensionless time variable
η	similarity variable
θ	dimensionless temperature
μ	dynamic viscosity (kg m^{-1}s^{-1})
ν	kinematic viscosity of the fluid (m^{2}s^{-1})
ρ	density of the fluid (kg m^{-3})
ψ	stream function
φ_1	nanoparticle volume fractions for magnetite
φ_2	nanoparticle volume fractions for cobalt ferrite
φ_{hnf}	hybrid nanoparticles volume fractions

Subscripts

f	base fluid
hnf	hybrid nanofluid
$n1$	solid component for magnetite
$n2$	solid component for cobalt ferrite

Superscript

$'$	differentiation with respect to η

Appendix A

The magnetic body force vector, **F** is defined by:

$$\mathbf{F} = \mathbf{J} \times \mathbf{B}$$

with the electric current vector, **J**:

$$\mathbf{J} = \sigma_{hnf}(\mathbf{E} + \mathbf{v} \times \mathbf{B}),$$

where σ_{hnf} is the electric conductivity and **E** is the electric field vector. It is assumed that the imposed magnetic field, $\mathbf{B} = \langle 0, 0, B* \rangle$, acts in the z-direction that is normal for the disk where the boundary layer is formed; the flow is confined to $z > 0$. Based on the flow assumption due to a low Reynolds number, the induced magnetic field can be neglected. Moreover, the electric field vector, **E**, is assumed to be zero, i.e., the electric and polarization effects are neglected. Therefore,

$$\mathbf{J} = \sigma_{hnf}(\mathbf{v} \times \mathbf{B}) = \sigma_{hnf}[\langle u, v, w \rangle \times \langle 0, 0, B* \rangle],$$

$$= \sigma_{hnf} \begin{vmatrix} \mathbf{i} & \mathbf{j} & \mathbf{k} \\ u & v & w \\ 0 & 0 & B* \end{vmatrix},$$

$$= \sigma_{hnf} \langle B*v, \ B*u, \ 0 \rangle,$$

where u, v, and w are the component velocities in the x, y, and z directions, respectively. Then, the expression $\mathbf{J} \times \mathbf{B}$ can be written as,

$$\mathbf{J} \times \mathbf{B} = \sigma_{hnf}[\langle B*v, \ B*u, \ 0 \rangle \times \langle 0, 0, B* \rangle],$$

$$= \sigma_{hnf} \begin{vmatrix} \mathbf{i} & \mathbf{j} & \mathbf{k} \\ B*v & B*u & 0 \\ 0 & 0 & B* \end{vmatrix},$$

$$= \sigma_{hnf} \langle B*^2 u, \ B*^2 v, 0 \rangle.$$

Thus,

$$(\mathbf{J} \times \mathbf{B})_x = \sigma_{hnf} B *^2 u, \qquad (\mathbf{J} \times \mathbf{B})_y = \sigma_{hnf} B *^2 v, \qquad (\mathbf{J} \times \mathbf{B})_z = 0,$$

where $(\mathbf{J} \times \mathbf{B})_x$, $(\mathbf{J} \times \mathbf{B})_y$, and $(\mathbf{J} \times \mathbf{B})_z$ are components of $\mathbf{J} \times \mathbf{B}$ in the x, y, and z directions, respectively.

References

1. Favre-Marinet, M.; Tardu, S. *Convective Heat Transfer*; ISTE Ltd.: London, UK, 2009.
2. Aljabali, A.; Kasim, A.R.M.; Arifin, N.S.; Isa, S.M. Mixed convection of non-newtonian erying powell fluid with temperature-dependent viscosity over a vertically stretched surface. *Comput. Mater. Contin.* **2021**, *66*, 421–435. [CrossRef]
3. Khalil, K.M.; Soleiman, A.; Megahed, A.M.; Abbas, W. Impact of Variable Fluid Properties and Double Diffusive Cattaneo–Christov Model on Dissipative Non-Newtonian Fluid Flow Due to a Stretching Sheet. *Mathematics* **2022**, *10*, 1179. [CrossRef]
4. Shehzad, N.; Zeeshan, A.; Shakeel, M.; Ellahi, R.; Sait, S.M. Effects of Magnetohydrodynamics Flow on Multilayer Coatings of Newtonian and Non-Newtonian Fluids through Porous Inclined Rotating Channel. *Coatings* **2022**, *12*, 430. [CrossRef]
5. Kasim, A.R.M.; Jiann, L.Y.; Shafie, S.; Ali, A. The effects of heat generation or absorption on MHD stagnation point of Jeffrey fluid. *AIP Conf. Proc.* **2014**, *1605*, 404–409.
6. Kasim, A.R.M.; Admon, M.A.; Shafie, S. Free convection boundary layer flow of a viscoelastic fluid in the presence of heat generation. *World Acad. Sci. Eng. Technol.* **2011**, *75*, 492–499.
7. Rawi, N.A.; Kasim, A.R.M.; Isa, M.; Shafie, S. G-Jitter induced mixed convection flow of heat and mass transfer past an inclined stretching sheet. *J. Teknol.* **2014**, *71*, 27–31. [CrossRef]
8. Kasim, A.R.M.; Arifin, N.S.; Zokri, S.M.; Ariffin, N.A.N.; Salleh, M.Z.; Anwar, M.I. Mathematical model of simultaneous flow between casson fluid and dust particle over a vertical stretching sheet. *Int. J. Integr. Eng.* **2020**, *12*, 253–260.
9. Aurangzaib Kasim, A.R.M.; Mohammad, N.F.; Shafie, S. Unsteady MHD mixed convection stagnation-point flow in a micropolar fluid on a vertical surface in a porous medium with soret and Dufour effects. *Heat Transf. Res.* **2013**, *44*, 603–620. [CrossRef]
10. Choi, S.U.S.; Eastman, J.A. Enhancing Thermal Conductivity of Fluids with Nanoparticles. In Proceedings of the ASME International Mechanical Engineering Congress and Exposition FED 231/MD, San Francisco, CA, USA, 12–17 November 1995; Volume 66, pp. 99–105.
11. Khanafer, K.; Vafai, K.; Lightstone, M. Buoyancy-driven heat transfer enhancement in a two-dimensional enclosure utilizing nanofluids. *Int. J. Heat Mass Transf.* **2003**, *46*, 3639–3653. [CrossRef]
12. Tiwari, R.K.; Das, M.K. Heat transfer augmentation in a two-sided lid-driven differentially heated square cavity utilizing nanofluids. *Int. J. Heat Mass Transf.* **2007**, *50*, 2002–2018. [CrossRef]
13. Oztop, H.F.; Abu-Nada, E. Numerical study of natural convection in partially heated rectangular enclosures filled with nanofluids. *Int. J. Heat Fluid Flow.* **2008**, *29*, 1326–1336. [CrossRef]
14. Hamad, M.A.A. Analytical solution of natural convection flow of a nanofluid over a linearly stretching sheet in the presence of magnetic field. *Int. Commun. Heat Mass Transf.* **2011**, *38*, 487–492. [CrossRef]
15. Hayat, T.; Rashid, M.; Alsaedi, A. MHD convective flow of magnetite-Fe3O4 nanoparticles by curved stretching sheet. *Results Phys.* **2017**, *7*, 3107–3115. [CrossRef]
16. Ganesh, N.V.; Hakeem, A.K.A.; Ganga, B. Darcy–Forchheimer flow of hydromagnetic nanofluid over a stretching/shrinking sheet in a thermally stratified porous medium with second order slip, viscous and Ohmic dissipations effects. *Ain Shams Eng. J.* **2018**, *9*, 939–951. [CrossRef]
17. Abbas, A.; Shafqat, R.; Jeelani, M.B.; Alharthi, N.H. Convective Heat and Mass Transfer in Third-Grade Fluid with Darcy–Forchheimer Relation in the Presence of Thermal-Diffusion and Diffusion-Thermo Effects over an Exponentially Inclined Stretching Sheet Surrounded by a Porous Medium: A CFD Study. *Processes* **2022**, *10*, 776. [CrossRef]
18. Waini, I.; Ishak, A.; Pop, I. Dufour and Soret effects on Al2O3-water nanofluid flow over a moving thin needle: Tiwari and Das model. *Int. J. Numer. Methods Heat Fluid Flow* **2021**, *31*, 766–782. [CrossRef]
19. Sulochana, C.; Samrat, S.P.; Sandeep, N. Boundary layer analysis of an incessant moving needle in MHD radiative nanofluid with joule heating. *Int. J. Mech. Sci.* **2017**, *128–129*, 326–331. [CrossRef]
20. Ellahi, R.; Zeeshan, A.; Hussain, F.; Abbas, T. Study of shiny film coating on multi-fluid flows of a rotating disk suspended with nano-sized silver and gold particles: A comparative analysis. *Coatings* **2018**, *8*, 422. [CrossRef]
21. Ellahi, R.; Sait, S.M.; Shehzad, N.; Ayaz, Z. A hybrid investigation on numerical and analytical solutions of electro-magnetohydrodynamics flow of nanofluid through porous media with entropy generation. *Int. J. Numer. Methods Heat Fluid Flow* **2020**, *30*, 834–854. [CrossRef]
22. Turkyilmazoglu, M. Natural convective flow of nanofluids past a radiative and impulsive vertical plate. *J. Aerosp. Eng.* **2016**, *29*, 04016049. [CrossRef]
23. Turkyilmazoglu, M. Nanoliquid film flow due to a moving substrate and heat transfer. *Eur. Phys. J. Plus* **2020**, *135*, 781. [CrossRef]
24. Estebe, C.; Liu, Y.; Vahab, M.; Sussman, M.; Moradikazerouni, A.; Shoele, K.; Guo, W. A Low Mach Number, Adaptive Mesh Method for Simulating Multi-phase Flows in Cryogenic Fuel Tanks. In Proceedings of the SIAM Conference on Computational Science and Engineering, Philadelphia, PA, USA, 25 August 2021.

25. Moradikazerouni, A.; Shoele, K.; Alireza Moradikazerouni Team; Kourosh Shoele Team. Computational study of RayleighBernard convection in a cylindrical pressurized cryogenic tank. *APS Div. Fluid Dyn. Meet. Abstr.* **2021**, F06.001.

26. Alireza, M. Heat transfer characteristics of thermal energy storage system using single and multi-phase cooled heat sinks: A review. *J. Energy Storage* **2022**, *49*, 104097.

27. Sidik, N.A.C.; Adamu, I.M.; Jamil, M.M.; Kefayati, G.H.R.; Mamat, R.; Najafi, G. Recent progress on hybrid nanofluids in heat transfer applications: A comprehensive review. *Int. Commun. Heat Mass Transf.* **2016**, *78*, 68–79. [CrossRef]

28. Turcu, R.; Darabont, A.; Nan, A.; Aldea, N.; Macovei, D.; Bica, D.; Vekas, L.; Pana, O.; Soran, M.L.; Koos, A.A.; et al. New polypyrrole-multiwall carbon nanotubes hybrid materials. *J. Optoelectron. Adv. Mater.* **2006**, *8*, 643–647.

29. Jana, S.; Salehi-Khojin, A.; Zhong, W.H. Enhancement of fluid thermal conductivity by the addition of single and hybrid nano-additives. *Thermochim. Acta* **2007**, *462*, 45–55. [CrossRef]

30. Suresh, S.; Venkitaraj, K.P.; Selvakumar, P.; Chandrasekar, M. Synthesis of Al2O3-Cu/water hybrid nanofluids using two step method and its thermo physical properties, Colloids Surfaces A Physicochem. *Eng. Asp.* **2011**, *388*, 41–48. [CrossRef]

31. Singh, S.K.; Sarkar, J. Energy, exergy and economic assessments of shell and tube condenser using hybrid nanofluid as coolant. *Int. Commun. Heat Mass Transf.* **2018**, *98*, 41–48. [CrossRef]

32. Farhana, K.; Kadirgama, K.; Rahman, M.M.; Noor, M.M.; Ramasamy, D.; Samykano, M.; Najafi, G.; Sidik, N.A.C.; Tarlochan, F. Significance of alumina in nanofluid technology: An overview. *J. Therm. Anal. Calorim.* **2019**, *138*, 1107–1126. [CrossRef]

33. Takabi, B.; Salehi, S. Augmentation of the heat transfer performance of a sinusoidal corrugated enclosure by employing hybrid nanofluid. *Adv. Mech. Eng.* **2014**, *6*, 147059. [CrossRef]

34. Chabani, I.; Mebarek-Oudina, F.; Ismail, A.A.I. MHD Flow of a Hybrid Nano-Fluid in a Triangular Enclosure with Zigzags and an Elliptic Obstacle. *Micromachines* **2022**, *13*, 224. [CrossRef] [PubMed]

35. Khan, U.; Waini, I.; Ishak, A.; Pop, I. Unsteady hybrid nanofluid flow over a radially permeable shrinking/stretching surface. *J. Mol. Liq.* **2021**, *331*, 115752. [CrossRef]

36. Khashi'ie, N.S.; Arifin, N.M.; Wahi, N.; Pop, I.; Nazar RHafidzuddin, E.H. Thermal marangoni flow past a permeable stretching/shrinking sheet in a hybrid Cu-Al2O3/water nanofluid. *Sains Malays.* **2020**, *49*, 211–222. [CrossRef]

37. Zainal, N.A.; Nazar, R.; Naganthran, K.; Pop, I. MHD flow and heat transfer of hybrid nanofluid over a permeable moving surface in the presence of thermal radiation. *Int. J. Numer. Methods Heat Fluid Flow.* **2021**, *31*, 858–879. [CrossRef]

38. Rizk, D.; Ullah, A.; Ikramullah; Elattar, S.; Alharbi, K.A.M.; Sohail, M.; Khan, R.; Khan, A.; Mlaiki, N. Impact of the KKL Correlation Model on the Activation of Thermal Energy for the Hybrid Nanofluid (GO+ZnO+Water) Flow through Permeable Vertically Rotating Surface. *Energies* **2022**, *15*, 2872. [CrossRef]

39. Imran, M.; Yasmin, S.; Waqas, H.; Khan, S.A.; Muhammad, T.; Alshammari, N.; Hamadneh, N.N.; Khan, I. Computational Analysis of Nanoparticle Shapes on Hybrid Nanofluid Flow Due to Flat Horizontal Plate via Solar Collector. *Nanomaterials* **2022**, *12*, 663. [CrossRef]

40. Waini, I.; Ishak, A.; Pop, I. Symmetrical solutions of hybrid nanofluid stagnation-point flow in a porous medium. *Int. Commun. Heat Mass Transf.* **2022**, *130*, 105804. [CrossRef]

41. Hassan, M.; Marin, M.; Ellahi, R.; Alamri, S.Z. Exploration of convecti ve heat transfer and flow characteristics synthesis by Cu-Ag/Water hybrid-nanofluids. *Heat Transf. Res.* **2018**, *49*, 1837–1848. [CrossRef]

42. Riaz, A.; Ellahi, R.; Sait, S.M. Role of hybrid nanoparticles in thermal performance of peristaltic flow of Eyring–Powell fluid model. *J. Therm. Anal. Calorim.* **2021**, *143*, 1021–1035. [CrossRef]

43. Sarkar, J.; Ghosh, P.; Adil, A. A review on hybrid nanofluids: Recent research, development and applications. *Renew. Sustain. Energy Rev.* **2015**, *43*, 164–177.

44. Babu, J.A.R.; Kumar, K.K.; Rao, S.S. State-of-art review on hybrid nanofluids. *Renew. Sustain. Energy Rev.* **2017**, *77*, 551–565. [CrossRef]

45. Huminic, G.; Huminic, A. Entropy generation of nanofluid and hybrid nanofluid flow in thermal systems: A review. *J. Mol. Liq.* **2020**, *302*, 112533. [CrossRef]

46. Yang, L.; Ji, W.; Mao, M.; Huang, J. An updated review on the properties, fabrication and application of hybrid-nanofluids along with their environmental effects. *J. Clean. Prod.* **2020**, *257*, 120408. [CrossRef]

47. Khan, Z.H.; Khan, W.A.; Qasim, M.; Shah, I.A. MHD stagnation point ferrofluid flow and heat transfer toward a stretching sheet. *IEEE Trans. Nanotechnol.* **2013**, *13*, 35–40. [CrossRef]

48. Qasim, M.; Khan, Z.H.; Khan, W.A.; Shah, I.A. MHD boundary layer slip flow and heat transfer of ferrofluid along a stretching cylinder with prescribed heat flux. *PLoS ONE* **2014**, *9*, e83930. [CrossRef] [PubMed]

49. Mehrez, Z.; Cafsi, A.E. Heat exchange enhancement of ferrofluid flow into rectangular channel in the presence of a magnetic field. *Appl. Math. Comput.* **2021**, *391*, 125634. [CrossRef]

50. Sekar, R.; Raju, K. Stability analysis of Soret effect on thermohaline convection in dusty ferrofluid saturating a Darcy porous medium. *Glob. J. Math. Anal.* **2015**, *3*, 37–48. [CrossRef]

51. Hamid, R.A.; Nazar, R.; Naganthran, K.; Pop, I. Dusty ferrofluid transport phenomena towards a non-isothermal moving surface with viscous dissipation. *Chin. J. Phys.* **2022**, *75*, 139–151. [CrossRef]

52. Goshayeshi, H.R.; Safaei, M.R.; Goodarzi, M.; Dahari, M. Particle size and type effects on heat transfer enhancement of ferro-nanofluids in a pulsating heat pipe. *Powder Technol.* **2016**, *301*, 1218–1226. [CrossRef]

53. Rashad, A.M. Impact of anisotropic slip on transient three dimensional MHD flow of ferrofluid over an inclined radiate stretching surface. *J. Egypt. Math. Soc.* **2017**, *25*, 230–237. [CrossRef]
54. Rashad, A.M. Impact of thermal radiation on MHD slip flow of a ferrofluid over a nonisothermal wedge. *J. Magn. Magn. Mater.* **2017**, *422*, 25–31. [CrossRef]
55. Wiriyasart, S.; Suksusron, P.; Hommalee, C.; Siricharoenpanich, A.; Naphon, P. Heat transfer enhancement of thermoelectric cooling module with nanofluid and ferrofluid as base fluids. *Case Stud. Therm. Eng.* **2021**, *24*, 100877. [CrossRef]
56. Ferdows, M.; Alam, J.; Murtaza, G.; Tzirtzilakis, E.E.; Sun, S. Biomagnetic Flow with CoFe2O4 Magnetic Particles through an Unsteady Stretching/Shrinking Cylinder. *Magnetochemistry* **2022**, *8*, 27. [CrossRef]
57. Jalili, B.; Jalili, P.; Sadighi, S.; Ganji, D.D. Effect of magnetic and boundary parameters on flow characteristics analysis of micropolar ferrofluid through the shrinking sheet with effective thermal conductivity. *Chin. J. Phys.* **2021**, *71*, 136–150. [CrossRef]
58. Hounsou, P.; Monwanou, A.V.; Miwadinou, C.H.; Orou, J.B.C. Effect of helical force on the stationary convection in a rotating ferrofluid. *Chin. J. Phys.* **2020**, *65*, 526–537. [CrossRef]
59. Bortnic, R.; Szatmari, A.; Souca, G.; Hirian, R.; Dudric, R.; Barbu-Tudoran, L.; Toma, V.; Știufiuc, R.; Tetean, R.; Burzo, E. New Insights into the Magnetic Properties of CoFe2O4@SiO2@Au Magnetoplasmonic Nanoparticles. *Nanomaterials* **2022**, *12*, 942. [CrossRef]
60. Nanjundappa, C.E.; Pavithra, A.; Shivakuamara, I.S. Effect of dusty particles on Darcy-Brinkman gravity-driven ferro-thermal-convection in a ferrofluid saturated porous layer with internal heat source: Influence of boundaries. *Int. J. Appl. Comput. Math.* **2021**, *7*, 1–20. [CrossRef]
61. Wang, W.; Timonen, J.V.I.; Carlson, A.; Drotlef, D.M.; Zhang, C.T.; Kolle, S.; Grinthal, A.; Wong, T.S.; Hatton, B.; Kang, S.H.; et al. Multifunctional ferrofluid-infused surfaces with reconfigurable multiscale topography. *Nature* **2018**, *559*, 77–82. [CrossRef]
62. Chu, Y.M.; Bilal, S.; Hajizadeh, M.R. Hybrid ferrofluid along with MWCNT for augmentation of thermal behavior of fluid during natural convection in a cavity. *Math. Methods Appl. Sci.* **2020**, *2020*, 1–12. [CrossRef]
63. Kumar, K.A.; Sandeep, N.; Sugunamma, V.; Animasaun, I.L. Effect of irregular heat source/sink on the radiative thin film flow of MHD hybrid ferrofluid. *J. Therm. Anal. Calorim.* **2020**, *139*, 2145–2153. [CrossRef]
64. Anuar, N.S.; Bachok, N.; Pop, I. Influence of MHD Hybrid Ferrofluid Flow on Exponentially Stretching/Shrinking Surface with Heat Source/Sink under Stagnation Point Region. *Mathematics* **2021**, *9*, 2932. [CrossRef]
65. Nabwey, H.A.; Mahdy, A. Transient flow of micropolar dusty hybrid nanofluid loaded with Fe3O4-Ag nanoparticles through a porous stretching sheet. *Results Phys.* **2021**, *21*, 103777. [CrossRef]
66. Tlili, I.; Mustafa, M.T.; Kumar, K.A.; Sandeep, N. Effect of asymmetrical heat rise/fall on the film flow of magnetohydrodynamic hybrid ferrofluid. *Sci. Rep.* **2020**, *10*, 6677. [CrossRef] [PubMed]
67. Giwa, S.O.; Sharifpur, M.; Goodarzi, M.; Alsulami, H.; Meyer, J.P. Influence of base fluid, temperature, and concentration on the thermophysical properties of hybrid nanofluids of alumina-ferrofluid: Experimental data, modeling through enhanced ANN, ANFIS, and curve fitting. *J. Therm. Anal. Calorim.* **2021**, *143*, 4149–4167. [CrossRef]
68. Kefeni, K.K.; Mamba, B.B.; Msagati, T.A.M. Magnetite and cobalt ferrite nanoparticles used as seeds for acid mine drainage treatment. *J. Hazard. Mater.* **2017**, *333*, 308–318. [CrossRef]
69. Von Kármán, T. Über laminare und turbulente Reibung, Zeitschrift Für Angew. *Math. Und Mech.* **1921**, *1*, 233–252.
70. Fang, T. Flow over a stretchable disk. *Phys. Fluids.* **2007**, *19*, 128105. [CrossRef]
71. Fang, T.; Zhang, J. Flow between two stretchable disks—An exact solution of the Navier-Stokes equations. *Int. Commun. Heat Mass Transf.* **2008**, *35*, 892–895. [CrossRef]
72. Turkyilmazoglu, M. MHD fluid flow and heat transfer due to a stretching rotating disk. *Int. J. Therm. Sci.* **2012**, *51*, 195–201. [CrossRef]
73. Turkyilmazoglu, M. Heat and mass transfer on the unsteady magnetohydrodynamic flow due to a porous rotating disk subject to a uniform outer radial flow. *J. Heat Transfer.* **2010**, *132*, 061703. [CrossRef]
74. Turkyilmazoglu, M. Unsteady flow over a decelerating rotating sphere. *Phys. Fluids.* **2018**, *30*, 033601. [CrossRef]
75. Watson, L.T.; Wang, C.Y. Deceleration of a rotating disk in a viscous fluid. *Phys. Fluids.* **1979**, *22*, 2267–2279. [CrossRef]
76. Watson, L.T.; Sankara, K.K.; Mounfield, L.C. Deceleration of a porous rotating disk in a viscous fluid. *Int. J. Eng. Sci.* **1985**, *23*, 131–137. [CrossRef]
77. Fang, T.; Tao, H. Unsteady viscous flow over a rotating stretchable disk with deceleration. *Commun. Nonlinear Sci. Numer. Simul.* **2012**, *17*, 5064–5072. [CrossRef]
78. Naganthran, K.; Mustafa, M.; Mushtaq, A.; Nazar, R. Dual solutions for fluid flow over a stretching/shrinking rotating disk subject to variable fluid properties. *Phys. A Stat. Mech. Its Appl.* **2020**, *556*, 124773. [CrossRef]
79. Sarkar, G.M.; Sahoo, B. On dual solutions of the unsteady MHD flow on a stretchable rotating disk with heat transfer and a linear temporal stability analysis. *Eur. J. Mech. B/Fluids.* **2021**, *85*, 149–157. [CrossRef]
80. Rafiq, T.; Mustafa, M. Computational analysis of unsteady swirling flow around a decelerating rotating porous disk in nanofluid. *Arab. J. Sci. Eng.* **2020**, *45*, 1143–1154. [CrossRef]
81. Waini, I.; Ishak, A.; Pop, I. Multiple solutions of the unsteady hybrid nanofluid flow over a rotating disk with stability analysis. *Eur. J. Mech. B Fluids* **2022**, *94*, 121–127. [CrossRef]
82. Merkin, J.H. On dual solutions occurring in mixed convection in a porous medium. *J. Eng. Math.* **1986**, *20*, 171–179. [CrossRef]

83. Weidman, P.D.; Kubitschek, D.G.; Davis, A.M.J. The effect of transpiration on self-similar boundary layer flow over moving surfaces. *Int. J. Eng. Sci.* **2006**, *44*, 730–737. [CrossRef]

84. Harris, S.D.; Ingham, D.B.; Pop, I. Mixed convection boundary-layer flow near the stagnation point on a vertical surface in a porous medium: Brinkman model with slip. *Transp. Porous Media.* **2009**, *77*, 267–285. [CrossRef]

85. Shampine, L.F.; Gladwell, I.; Thompson, S. *Solving ODEs with MATLAB*; Cambridge University Press: Cambridge, UK, 2003.

86. Shampine, L.F.; Kierzenka, J.; Reichelt, M. Solving boundary value problems for ordinary differential equations in MATLAB with bvp4c. *Tutor. Notes* **2000**, *2000*, 1–27.